TXRF Spectrometry for Investigating CaF_2:$Nd^{3+}Y^{3+}$ Nanoparticle Diffusion in Tumoral Cancer 3D Spheroids

Ramón Fernández-Ruiz *, Pablo Camarero Linares, Patricia Haro-Gonzalez, Marta Quitanilla

Posted Date: 15 February 2026

doi: 10.20944/preprints202602.1118.v1

Keywords: TXRF; nanoparticles; CaF_2: Nd^{3+},Y^{3+}, cell spheroids; adenocarcinoma; MCF-7; glioblastoma; U-87 MG; cellular uptake; internalisation; difussion

 doi:10.20944/preprints202602.1118.v1

Article

TXRF Spectrometry for Investigating CaF_2:$Nd^{3+}Y^{3+}$ Nanoparticle Diffusion in Tumoral Cancer 3D Spheroids

Ramón Fernández-Ruiz [1,*], Pablo Camarero Linares [2], Patricia Haro González [2] and Marta Quintanilla [2]

[1] Servicio Interdepartamental de Investigación (SIdI), Facultad de Ciencias, Universidad Autónoma de Madrid, Cantoblanco, 28049 Madrid, Spain

[2] Departamento de Física de Materiales, Facultad de Ciencias, Universidad Autónoma de Madrid, Cantoblanco, 28049 Madrid, Spain

* Correspondence: ramon.fernandez@uam.es

Abstract

Understanding the interactions of nanomaterials with complex tumour models is essential for advancing their use in nanomedicine. Calcium fluoride nanoparticles doped with neodymium and yttrium (CaF_2:Nd^{3+}, Y^{3+}) exhibit promising properties for biomedical applications, particularly for optical sensing and tagging. This study investigates their interaction with 3D cell spheroids derived from breast cancer (MCF-7) and brain cancer (U-87 MG) cell lines as tumour models. Specific protocols have been developed in Total-reflection X-Ray Fluorescence (TXRF) to evaluate nanoparticles' internalisation and diffusion within spheroids by quantifying the concentrations of Ca, Nd, and Y taken up by the cells. Minimal background interference enabled precise multi-element detection in low-volume biological samples, yielding very low detection limits and minimal uncertainties. The study demonstrates the effectiveness of TXRF for quantifying rare-earth-doped nanoparticles in 3D cancer models and reveals that, although both cell lines permit nanoparticle diffusion into cells, higher accumulation is observed in glioblastoma cell spheroids. A Weibull diffusion model was applied to help understand the observed internalisation kinetics of nanoparticles into U-87 MG and MCF-7 spheroids. The relevant differences suggest cell-line-dependent uptake behaviour, potentially influenced by differences in cellular architecture, the porosity of the generated spheroid, and its intercellular 3D microstructure. These findings highlight the importance of tumour-specific interactions in the investigation of nanoparticle systems for targeted cancer diagnostics and therapeutics.

Keywords: TXRF; nanoparticles; CaF_2:Nd^{3+},Y^{3+}, cell spheroids; adenocarcinoma; MCF-7; glioblastoma; U-87 MG; cellular uptake; internalisation; difussion

1. Introduction

Rare-earth-doped nanoparticles (NPs) are increasingly recognised as valuable tools in nanomedicine for their distinctive optical properties, chemical stability, and low cytotoxicity [1]. Moreover, electronic shielding produces narrow emission bands, enabling deconvolution from other luminescent signals and making them valuable as optical sensors. Among these, calcium fluoride nanoparticles doped with neodymium and yttrium (CaF_2:Nd^{3+}, Y^{3+}) have been demonstrated for thermal sensing applications and as near-infrared optical labels [2,3].

To assess their suitability in biomedicine, it is essential to study their interactions with biologically relevant models. Three-dimensional (3D) cell spheroids provide an advanced in vitro system that more closely replicates the architecture and microenvironment of solid tumours than conventional 2D cultures. As 3D structures, spheroids exhibit gradients of oxygen, nutrients, and pH,

 doi:10.20944/preprints202602.1118.v1

as well as realistic cell–cell and cell–matrix interactions, making them well-suited for evaluating nanoparticle diffusion kinetics in a more realistic manner [4]. In this study, breast cancer (most likely adenocarcinoma) spheroids (MCF-7) and brain cancer (most likely glioblastoma) spheroids (U-87 MG) were selected as representative models of two clinically significant cancer types with distinct biological characteristics. Understanding the extent to which CaF_2:Nd^{3+},Y^{3+} NPs interact with these 3D systems provides insights into cellular uptake, retention, and elemental distribution.

Since the ultimate application of these NPs is as optical sensors, mainly for thermometry, it is essential to quantify the amount of material internalised by the cells. NPs' concentration in the sample directly affects the emission signal-to-noise ratio, which must be carefully evaluated and optimised to ensure reliable temperature readouts. A low internalised dose may result in insufficient signal, whereas excessive uptake can induce cytotoxic effects. Therefore, understanding the rules governing the material's entry into the spheroids is a critical step in optimising nanosensor performance.

To investigate the NPs-spheroid interactions, Total-reflection X-Ray Fluorescence (TXRF) was employed for the first time with this nanoparticle type. TXRF is a highly sensitive, multi-elemental technique capable of detecting trace amounts of calcium, neodymium and yttrium in biological samples. It requires minimal sample preparation and provides quantitative elemental analysis with excellent precision, making it particularly suitable for nanoparticle tracking in complex cell models. TXRF is widely applied across diverse scientific fields, including catalysis, biochemistry, materials science, and archaeometry [5–17], among others. In fact, previous studies have demonstrated its effectiveness for nanoparticle analysis and bio-sample quantification [18–24], highlighting its versatility and analytical robustness. Regarding nanoparticle interactions with biological samples, several applications are available, mostly focusing on Au nanoparticles and their detection in blood [25], quantification of cytotoxicity in cancer cells [26,27], or detection of their presence in tissues [21,28]. Work on spheroids is scarce and is limited to μ-XRF for nanoparticle localisation [29,30]. However, the sensitivity of TXRF enables accurate quantification of the total nanoparticle load within cell aggregates, information that becomes increasingly relevant as 3D spheroids are used as an intermediate model between monolayer culture and in vivo studies.

Working with three-dimensional samples (tissues) is challenging and has been addressed by lyophilisation [21] or by histological sections [28], and has been applied to the detection of gold nanoparticles. With this idea in mind, the main goal of this work is to develop a rapid microanalytical method to quantify the uptake of CaF_2:Nd^{3+},Y^{3+} NPs and to compare their interactions in breast and glioma spheroids. To do this, we have considered the most relevant parameters to describe the incubation treatments, the time and nanoparticle concentration applied. These findings will contribute to a better understanding of nanoparticle interactions in tumour-like environments and support their potential application in cancer nanotheranostics. To our knowledge, this is the first report of TXRF being used to study nanoparticle uptake in complete 3D spheroid systems.

2. Experimental

2.1. Instrumentation

Qualitative and quantitative TXRF analyses were performed with a benchtop S2 PicoFox TXRF spectrometer from Bruker Nano (Germany), equipped with a Mo X-ray source working at 50 kV and 600 μA, a multilayer monochromator with 80 % of reflectivity at 17.5 keV (Mo Kα), an XFlash SDD detector with a functional area of 30 mm^2 and an energy resolution better than 150 eV for 5.9 keV (Mn Kα). The commercial Spectra v.7.8.2 software package from Bruker was used for deconvolution, integration, and quantification. All the reagents used in this work were of suprapure quality. The ultrapure water used in this study was from a Milli-Q Element system (18.2 MΩ) from Millipore (France). Microscopic images were obtained using a Nikon SMZ-800 binocular microscope. The micro-X-Ray Fluorescence (μ-XRF) spectrometer used in this study was the M4 Tornado (Bruker, Germany), equipped with a 30W microfocus Rh X-ray tube and a polycapillary lens, yielding a spot size of approximately 20 μm. XRF detection was performed using an SDD with a 30 mm^2 detection

 doi:10.20944/preprints202602.1118.v1

area and an energy resolution of better than 145 eV for Mn Kα (5.9 keV). Mappings were performed using a step size of 25 µm and a time per step of 30 ms/pixel. The X-ray tube was operated at 50 kV and 500 µA without using a filter.

2.2. Sample Preparation

2.2.1. Synthesis of $CaF_2:Nd^{3+},Y^{3+}$ NPs

The nanoparticles were synthesised using the hydrothermal method in a pressurised autoclave, as originally developed by Pedroni et al. [31] and recently modified by some of the authors [2]. These previous studies have shown that this synthesis produces citrate-stabilised nanoparticles of 14 ± 3 nm in size, with a homogeneous cubic phase, resulting in a cubic morphology (see Figure 1).

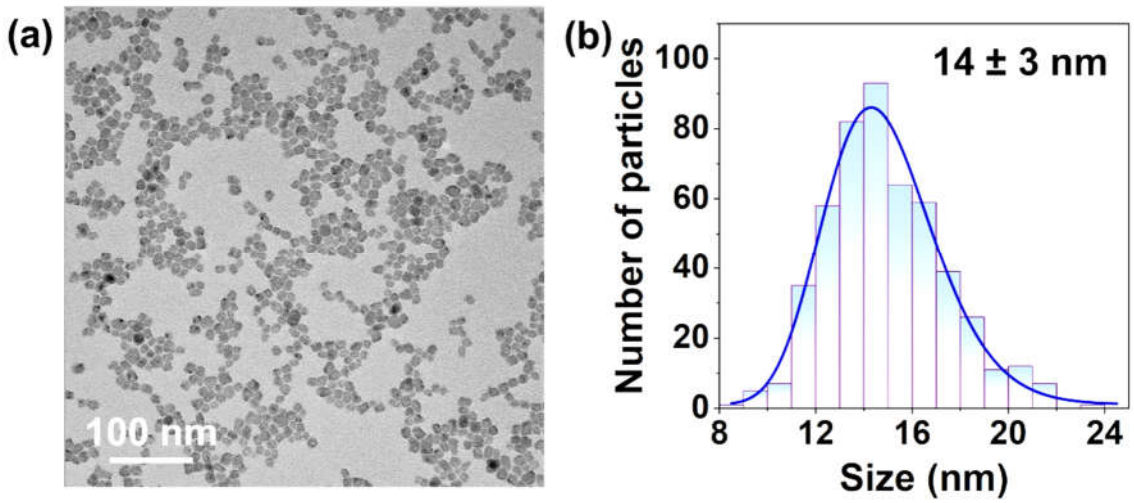

Figure 1. (a) TEM image illustrating the morphology and dimensions of the $CaF_2:Nd^{3+},Y^{3+}$ NPs. (b) Corresponding particle size distribution obtained from 500 measurements and fitted with a log-normal function to estimate the nanoparticle diagonal size.

The synthesis has been developed using calcium chloride dihydrate (>99%, Panreac), yttrium (III) chloride hexahydrate (99.99 %, Sigma-Aldrich), ammonium fluoride (98%, Acros) and neodymium (III) chloride hexahydrate (99.9 %, Sigma-Aldrich) as precursors and sodium citrate tribasic dihydrate (99.0 %, Panreac) as capping agent. All chemicals were purchased without further purification, and Milli-Q water was used as the solvent.

2.2.2. Cell Culture

Cell experiments were performed using human glioblastoma epithelial cells (U-87 MG) and human breast adenocarcinoma cells (MCF-7). Both cell lines were maintained in DMEM supplemented with 10% Fetal Bovine Serum (FBS) and 1% penicillin–streptomycin (P/S), all obtained from ThermoFisher. Cultures were incubated at 37 °C in a Midi 40 incubator under 5% CO_2 conditions.

2.2.3. Spheroid's Growth and Incubation Protocol

To investigate the influence of incubation time and exposure concentration on $CaF_2:Nd^{3+}$, Y^{3+} NPs, 3D spheroids were developed from both cell lines using a forced-floating method. From 2D cell culture, the cell density (cells/mL) was estimated using a Neubauer chamber. Approximately 4000 cells were plated in an ultra-low-attachment (ULA) U-bottom 96-well plate (FaCellitate) in 200 µL of complete cell culture medium on day 0. On day two (48 hours later), the spheroids were compact and could be easily handled and incubated with NPs. To do so, after removing all cell culture medium, 200 µL of the desired NP concentration in complete DMEM is added to each well. These

 doi:10.20944/preprints202602.1118.v1

concentrations and incubation times depend on the experiment. Incubation time was set to 48 h, whereas concentration was varied; a concentration of 164 ppm (mg/L) was used in the incubation time variation experiment. Finally, the spheroids were washed twice with 200 µL of Phosphate-Buffered Saline (PBS) to remove residual NPs from the surrounding medium. To prepare samples for TXRF analysis, the desired number of spheroids in PBS was transferred to an Eppendorf tube. To remove PBS, spheroids were washed twice with 200 µL of Milli-Q water, with the washes performed rapidly to preserve spheroid integrity. Finally, spheroids were resuspended in Milli-Q water for TXRF measurement. Figure 2 illustrates the spheroids development and the NPs' incubation process.

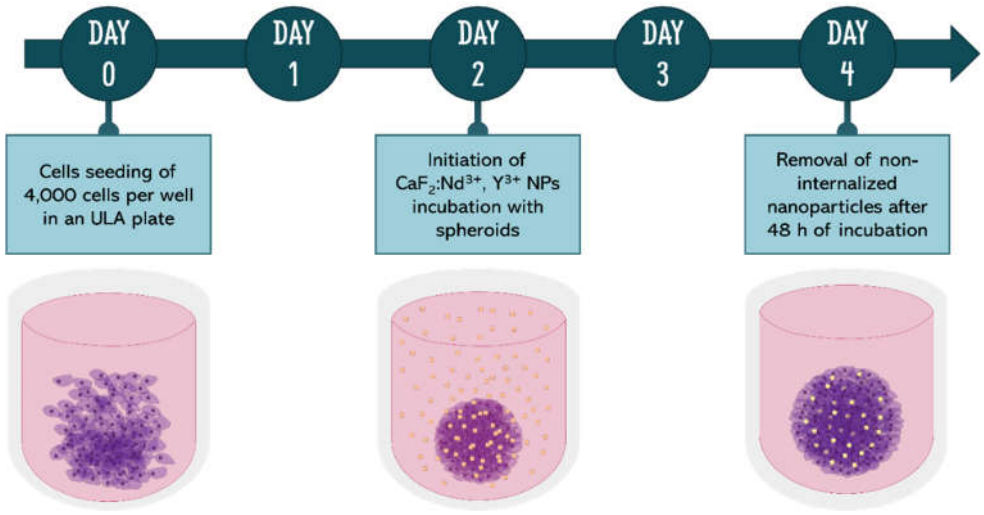

Figure 2. Scheme of the spheroid growth and NPs incubation process for experiments where the incubation time was fixed at 48 h. Longer incubation times also began on day 2, but the cell medium containing NPs was removed at a different time.

2.2.4. Spheroids' Incubation with Nanoparticles

Despite optimisation of culture protocols, spheroids can exhibit heterogeneity arising from minor cell aggregation during plating, well defects, and other factors. Thus, multiple *m* replicates were included in all experiments, allowing the internalisation values to be averaged. In addition, more spheroids than necessary were always grown, allowing defects to be discarded on Day 2. To evaluate uptake, 20 spheroids of each cell line were incubated separately with four different NPs concentrations: 1000 ppm (m = 4), 750 ppm (m = 8), 500 ppm (m = 4), and 200 ppm (m = 4). Subsequently, spheroids were introduced in groups of four into separate vials for analysis. This results in one sample per concentration; however, for 750 ppm, a duplicate was included to assess the repeatability of TXRF measurements throughout the process. The same protocol was followed with the MCF-7 cell line.

Each set of samples was completed with a control sample of untreated spheroids, to provide information on any possible background signal. In the MCF-7 experiment, the control sample contains three spheroids in 100 µL of water. In U-87 MG, three different control samples were included: C1 (m = 1) in 20 µL of water, C3 (m = 3) in 60 µL of water and C5 (m = 5) in 100 µL of water. This control set, which varies the number of spheroids per sample, enables evaluation of TXRF analytical parameters, such as linearity and sensitivity.

To analyse nanoparticle internalisation over time, 5 spheroids from each cell line were selected and treated individually for each condition. All treatments were performed at a fixed NPs concentration of 164 ppm, except for the untreated control samples. Spheroids were washed at 7 time points: 2, 4, 8, 16, 24, 48, and 72 h to stop the internalisation process. To proceed with TXRF experiments, the spheroids that underwent the same treatment (m = 5) were transferred to Eppendorf vials with 100 µL of water, including the control sample. Accordingly, 35 MCF-7 spheroids and 40 U-

 doi:10.20944/preprints202602.1118.v1

87 MG spheroids were analysed, as the 2 h condition was repeated in the glioblastoma cell line to assess the reproducibility of the process.

2.2.5. Spheroids Micro-Digestion and Standardisation

Following the previous incubation and nanoparticle washing protocol, 1 to 5 spheroids were micro-digested in each sample using suprapure nitric acid. The volume of HNO_3 added was equal to the volume of water already present in the sample (20, 60, 80, or 100 µL). Then, the resulting samples were digested in a boiling water bath at 100 °C for 2 hours, with the hot plate set to 120 °C. Figure 3 shows an image of the home-designed micro-digestion system used to acid-digest the cell spheroids and any remaining protein-rich cell culture medium.

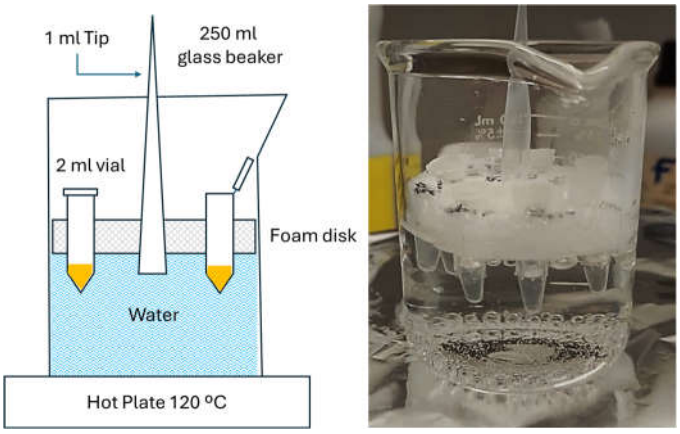

Figure 3. Home-designed micro-digestion system including a boiling water bath to prepare the spheroid samples for TXRF.

Once cooled, samples were standardised by adding 1 ppm of Ga as an internal standard (IS) in the same volume as the starting sample. This procedure resulted in a final dilution factor of three, reducing the Ga concentration to 0.333 ppm. In this way, the same factor three turns out to be the dilution factor applied to the initial concentrations of all elements present in the cell spheroids. Thus, during TXRF sample processing, Ga concentration 333 ppb (ng/mL) was renormalised to 1 ppm, allowing all elemental concentrations to be calculated relative to the original volume, *V*, of the cleaned spheroids. Figure 4 summarises the complete workflow, including digestion, standardisation, and preparation for TXRF analysis.

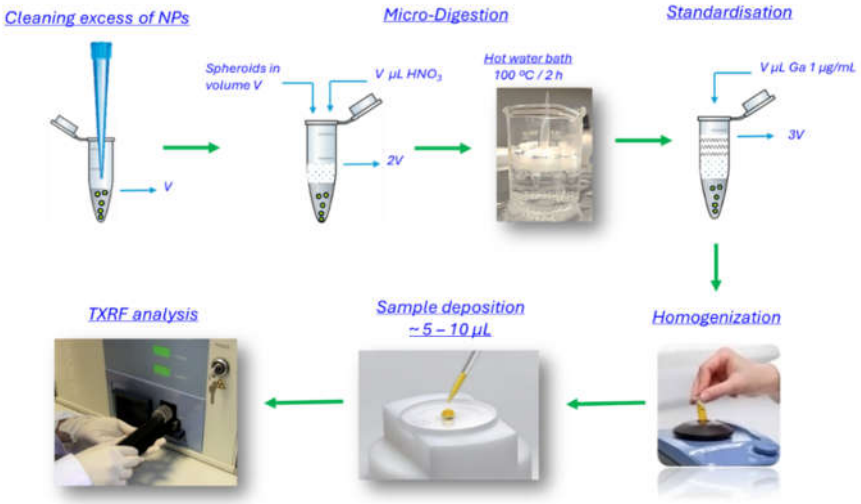

Figure 4. Scheme of the micro-digestion and standardisation process of the analysed samples.

 doi:10.20944/preprints202602.1118.v1

3. Results and Discussion

3.1. Qualitative Evaluation

After complete digestion of the spheroids, the samples were qualitatively evaluated. Figure 5 shows the obtained spectra of U-87 MG and MCF-7 spheroids, pure and treated with $CaF_2:Nd^{3+},Y^{3+}$ NPs.

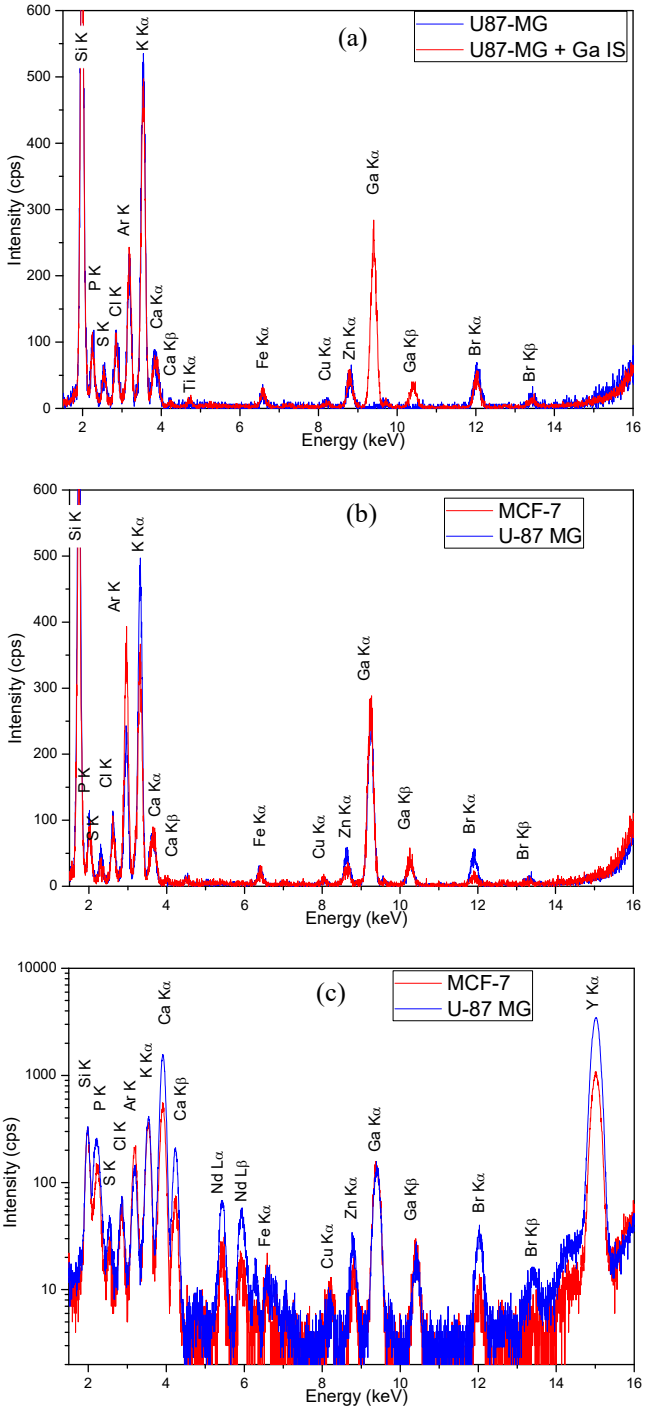

Figure 5. (a) Comparison of the elemental profile of U-87 MG cell spheroids incubated in the same way with (red) and without (blue) Ga spiked as an IS. (b) Comparison of the elemental profile detected of U-87 MG (blue) and MCF-7 (red) for three spheroids. (c) Comparison of the TXRF spectra of U-87 MG spheroids (blue) and MFC-7 spheroids (red) exposed to 750 ppm of $CaF_2:Nd^{3+},Y^{3+}$ NPs for 48 h, digested and standardised with 333 ppb of Ga, both normalised to the K_α signal of Ga.

 doi:10.20944/preprints202602.1118.v1

The elemental profiles observed by TXRF are very similar between the two spheroid types, U-87 MG and MCF-7. Figure 5a presents the elemental profile of U-87 MG cell spheroids incubated in the same way with (red) and without (blue) Ga spiked as IS, showing that it does not interfere with any other elements from the sample. Figure 5b displays the comparison of the elemental profile detected in U-87 MG (blue) and MCF-7 (red). Spectra show that the TXRF spectral lines of the elements associated with the samples, likely including traces of cell culture medium, PBS and the intracellular contents of U-87 MG and MCF-7 spheroids, were P-$K_{\alpha\beta}$, S-$K_{\alpha\beta}$, Cl-$K_{\alpha\beta}$, K-$K_{\alpha\beta}$, Ca-$K_{\alpha\beta}$, Ti-$K_{\alpha\beta}$, Fe-$K_{\alpha\beta}$, Cu-$K_{\alpha\beta}$, Zn-$K_{\alpha\beta}$, and Br-$K_{\alpha\beta}$. Additionally, Si-$K_{\alpha\beta}$, Ar-$K_{\alpha\beta}$, and Ga-$K_{\alpha\beta}$ are present due to the quartz reflector, the air in the total-reflection chamber, and the internal standard, respectively. These spectra (Figure 5b) also indicate that the elemental profile is identical for both U-87 MG and MCF-7 tumoral cell spheroids. However, the abundance of certain elements varies significantly across cell lines, with S, Zn, and Br being lower in breast cancer than in glioblastoma.

Figure 5c shows the comparative TXRF spectra of the digested samples of U-87 MG (red) and MFC-7 (blue) spheroids treated with 750 ppm of CaF_2:Nd^{3+}, Y^{3+} NPs for 48 h, normalised to the Kα signal of the IS added. The comparison indicates the high analytical sensitivity of TXRF for detecting CaF_2:Nd^{3+}, Y^{3+} NPs within the investigated cell spheroids. The highly resolved Ca-K$\alpha\beta$, Nd-L, and Y-K$\alpha\beta$ signals are clearly observed in both spectra. Additionally, a significant difference in the quantity of CaF_2:Nd^{3+}, Y^{3+} NPs is observed, as indicated by the intensity of signals related to the NPs' components (Ca, Nd and Y). This qualitative approximation suggests that these elements are more abundant in glioma spheroids than in breast cancer spheroids.

3.2. Evaluation of the Control Samples

Three control samples of the glioblastoma U-87 MG cell line were specifically prepared to test the ability of TXRF to detect and quantify the cellular elemental composition. Control samples C1, C3, and C5 include 1, 3, and 5 U-87 MG cell spheroids, respectively, resuspended in 20 µL, 60 µL, and 100 µL of water. Figure 6a shows the results obtained after sample preparation, as previously described (section 2.2.2). The elements P, S, Cl and K increase proportionally with the number of spheroids evaluated, indicating that they are correlated with the cellular composition of the U-87 MG cell spheroids. This observation is consistent with previous studies on cancer tissues, which demonstrate that TXRF is particularly sensitive to light elements in cells, such as P and S [8]. Interestingly, this technique has also shown that increased levels of K and, to a lesser extent, Cl are present in some cancer cells, distinguishing them from healthy tissues [9].

The remaining elements show only aleatory variations, suggesting they may also be linked to other uncontrolled sources, including traces of cell culture medium and PBS. Notably, Y and Nd were not detected in these samples; their concentrations are below the detection limits of 7 and 22 ppb, respectively. Ca was detected in the blank with a concentration level of 0.64 ppm in the control C5 sample, indicating a negligible blank signal (< 2%) for all cases evaluated in this work where NPs were quantified.

The linear correlation between the concentrations of the elements P, S, Cl, and K and the number of spheroids (and thus, cells) is shown in Figure 6b. This trend verifies several aspects: first, the ability of TXRF spectrometry to quantify intracellular elements. Second, the high values of the correlation factors achieved, ranging from 0.947 to 0.999, point to a linear dependency between the TXRF signal and the number of spheroids, which can eventually be used as a rough indication of the number of cells in the experiment, with K and P being the most sensitive elements. This, though, must be taken with care, as the exact composition of the cells may vary between batches, because it relates to cell metabolism and ageing. Third, interpolation to zero spheroids reveals residual traces of cell culture medium and PBS (blank), with P=9.22 ppm, S=3.54 ppm, Cl=2.75 ppm, and K=10.34 ppm, as indicated by the fitted equations.

 doi:10.20944/preprints202602.1118.v1

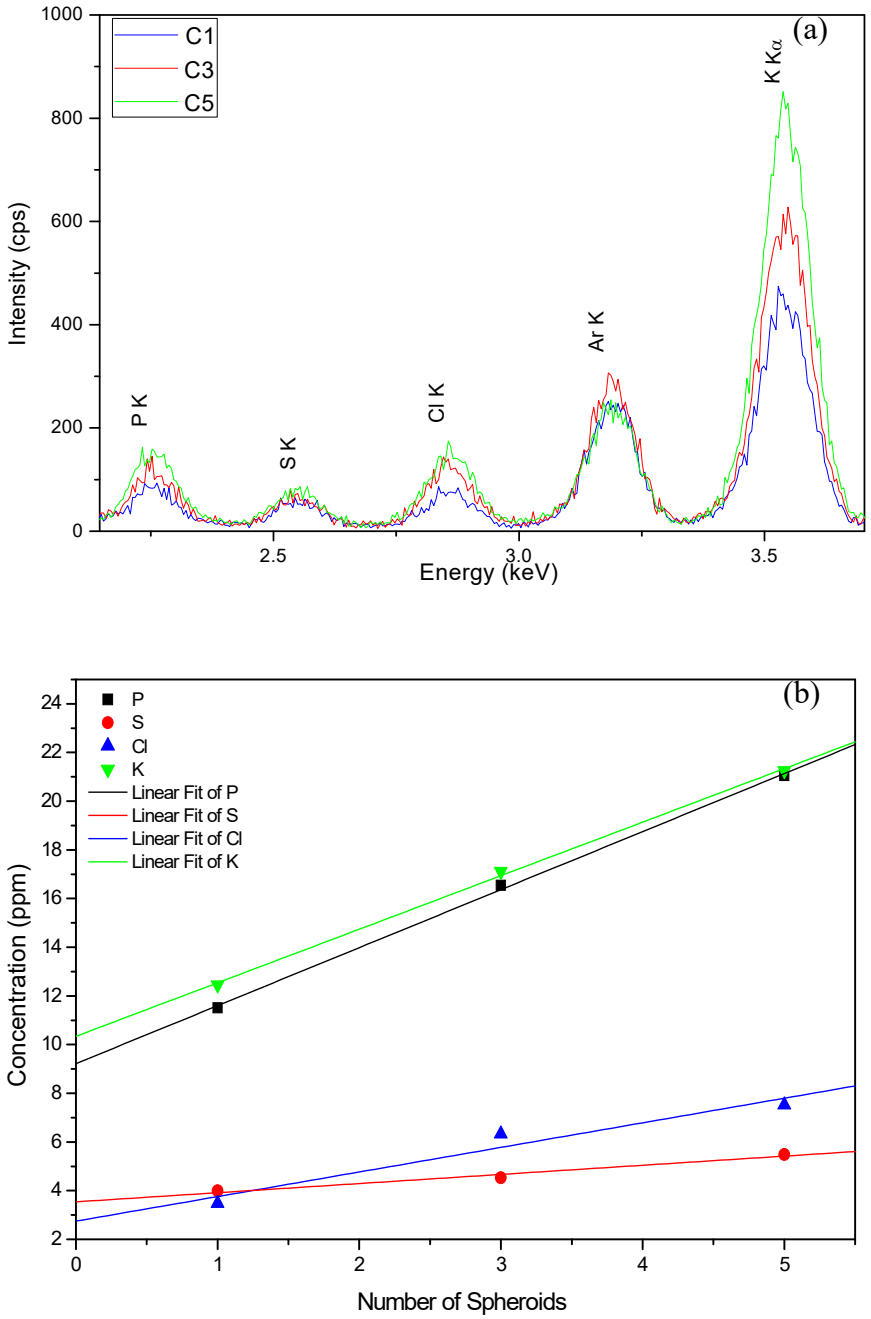

Figure 6. (a) Comparative spectra for 1 (blue), 3 (red) and 5 (green) U-87 MG spheroids, normalised to the Ga signal. (b) Linear correlation of the concentrations of the elements P, S, Cl and K versus the number of spheroids (cells) evaluated.

3.3. Analytical Parameters

3.3.1. Average Concentrations and Detection Limits

So far, we have observed that the detected elements are qualitatively derived from two primary sources. The first group, Ca, Nd, and Y, comprises the NPs investigated in the concentration-exposure and incubation-time experiments. The second group, P, S, K, Ca, Fe, Cu, and Zn, is derived from the cellular composition of the spheroids, supplemented by induction from the culture medium and from PBS.

On this basis established for spheroid analysis, we can now proceed to quantify NP internalisation. It must be noted, though, that the halogens Cl and Br are not present now due to their

 doi:10.20944/preprints202602.1118.v1

aleatory loss by evaporation in the acid digestion and IS addition. The average concentrations obtained in parallel for three samples of U-87 MG spheroids exposed to 750 ppm of CaF_2:Nd^{3+}, Y^{3+} NPs were used in this part of the study. Table 1 presents the average values, coefficients of variation (CVs), and detection limits (DLs). Detection limits were calculated by using the adaptation of the Poisson statistic to the counting measurement shown in Equation (1)

$$DL_x = 3\frac{C_x}{N_x}\sqrt{N_B}\ , \qquad (1)$$

where C_x is the concentration of element x, associated with its net peak intensity N_x and the background intensity N_B, both expressed as net counts.

Table 1. Average concentration *C*, coefficient of variation *CV* and detection limits *DL* obtained for the sample of U-87 MG glioblastoma spheroids (*n*=3) exposed to 750 ppm of NPs during 48 h.

Element	*C (μg/ml)*	*CV (%)*	*DL (μg/ml)*
Ca	27.46	0.741	0.13
Y	5.29	0.091	0.02
Nd	0.95	0.035	0.05
P	34.60	1.85	1.11
S	2.74	0.360	0.62
K	22.00	0.845	0.17
Fe	0.100	0.021	0.021
Cu	0.050	0.017	0.011
Zn	0.090	0.019	0.009

The first group (Ca, Nd, Y) coming from the investigated nanoparticles obtain relatively low concentrations compared to endogenous elements such as P and K. Detection limits are quite low for most elements, ranging from 9 ppt (ng/mL) for Zn to 1.11 ppm for P, showing the high sensitivity of the TXRF technique for this analytical application. If we compare detection limits with average concentrations, we always obtain a concentration above the detection limit. In the case of Ca, a concentration of 27.46 ppm was observed, after subtracting the blank values, with a DL of 0.13 ppm, indicating that the detected signal is well above the detection threshold in all cases. P has the highest concentration (34.56 ppm), whereas its detection limit (1.11 ppm) is relatively high compared with the others. This observation is attributable to P's lower sensitivity, evidenced by its low-energy K_α fluorescence signal at 2.01 keV. Ca and K also exhibit high concentrations and low detection limits, indicating high detectability. Trace elements such as Cu, Zn, and Fe have very low concentrations, but detection limits are even lower, suggesting they remain measurable with good sensitivity for evaluating cellular media contents.

3.3.2. CaF_2:Nd^{3+}, Y^{3+} NPs Stoichiometry Recoveries

The CaF_2: Nd^{3+}, Y^{3+} NPs were synthesised to obtain a molar ratio of 1:0.1:0.01 for CaF_2:Y:Nd, respectively. This relation implies a theoretical mass proportion of 88.3:10.05:1.6 wt%, respectively. Based on this data, TXRF was used to determine the stoichiometry of the synthesised nanoparticles under investigation. Two groups of aleatory samples were measured: first, seven samples of glioblastoma spheroids exposed to different concentrations of CaF_2:Nd^{3+}, Y^{3+} NPs; and second, a group of five samples from different NP syntheses in aqueous solution to estimate their stoichiometry without distortion from bioaccumulation or digestion. Table 2 shows the achieved results.

 doi:10.20944/preprints202602.1118.v1

Table 2. Average stoichiometric NPs concentration *C (wt%)*, standard deviation *sd (wt%)*, coefficient of variation *CV (%)* and Recoveries (%) obtained for different glioblastoma spheroids (n=7) (Up) and for different NPs synthesis in suspension (n=5) (Down).

	Element	*Theo (wt%)*	*C (wt%)*	*sd (wt%)*	*CV (%)*	*Recovery (%)*
Exposed NPs Glioblastoma Spheroids	CaF_2	88.3	88.7	1.3	1.5	100.5
	Y	10.0	9.6	1.1	11.3	96.0
	Nd	1.6	1.7	0.3	15.3	106.3
Syntesized NPs Suspension	CaF_2	88.3	87.4	0.6	0.7	99.0
	Y	10.0	10.9	0.6	5.5	109.0
	Nd	1.6	1.7	0.2	11.4	106.3

The results obtained in Table 2 indicate a perfect correlation between the theoretical NPs composition and the TXRF analytical results. Recoveries ranging from 96% to 109% for the three phases of the NPs matrix (CaF_2, Nd, and Y) constitute a strong test of this aspect of the TXRF measurements. The uncertainties were evaluated as coefficients of variation (CVs) in per cent and showed a clear dependence on concentration, with lower CVs at higher concentrations. Comparing the NPs after incubation and digestion with those directly synthesised in suspension, it is evident that there are no analytical differences. So, the comparison between the CaF_2, Y and Nd results of both groups, NPs bioaccumulated in U-87 MG spheroids and NPs directly synthesised, is statistically equivalent considering only one standard deviation (see Table 2). The analytical results were as follows: for CaF_2 wt% results, 88.7 ± 1.3 versus 87.4 ± 0.6; for Y wt% results, 9.6 ± 1.1 versus 10.9 ± 0.6; and for Nd wt% results, 1.7 ± 0.3 versus 1.7 ± 0.2.

3.3.3. Recoveries by Spike Addition

In a broader context, spike-and-recovery validation is a technique used to assess the accuracy and recovery of analytical methods by adding a known amount of an analyte to a sample matrix. This method helps evaluate the performance of the analytical procedure in the presence of potential matrix effects or when applied to new matrices in analytical research. The spike recovery percentage is a good indicator of the method's accuracy in analytical methodology [32]. This aspect is particularly relevant in our case, because there are no certified reference materials for CaF_2:Nd^{3+},Y^{3+} NPs interacting with these specialised matrices, MCF-7 and U-87 MG. Therefore, to evaluate the recovery percentage of the Ca and Y constituents, two glioblastoma samples exposed to 750 ppm of NPs were used. After digestion, both samples were spiked with 5 ppm of Ca and Y using monoelemental standards with certified nominal concentrations of 1000 ppm from SCP Sciex (Ontario, Canada). Nd was not added because no suitable monoelemental reference standard was available. In these conditions, the average recoveries achieved were 109% and 102% for Ca and Y, respectively. Given that both values are close to 100%, we can assume negligible matrix interference and high analytical TXRF accuracy.

3.3.4. Uncertainty Evaluation

Once the methodology was characterised, experiments were conducted to evaluate three primary uncertainty sources in TXRF measurements: instrumental uncertainty (U_{ins}), roughness uncertainty (U_{Rough}), and methodological uncertainty (U_{meth}). The uncertainties were assessed following the works of Fernandez-Ruiz [33,34]. In this method, TXRF empirical expanded uncertainties, U_x, expressed as a percentage for each element, x, can be evaluated with a 95% success probability (k=2) as

$$U_x = \frac{100}{C_x}\sqrt{\frac{4}{n(n-1)}\sum_{i=1}^{n}\left(C_x^i - C_x\right)^2} \quad , \qquad (2)$$

where C_x is the average concentration value for element x, n is the sampling order, and C^i_x is each concentration value obtained for element x. The instrumental uncertainty, U_{Ins}, quantifies variability

 doi:10.20944/preprints202602.1118.v1

arising from the spectrometer, mechanical stability, acquisition spectra, the deconvolution algorithm, and other spectrometer parameters. To evaluate it, one deposition was analysed three times (n=3), with the reflector introduced and removed between measurements to adequately account for mechanical stability. Roughness uncertainty (U_{Rough}) informs about microscopic inhomogeneities in the sample deposited on the TXRF reflectors. It can be calculated by analysing the same sample deposition at different relative positions between the reflector's surface and the X-ray beam source. This was achieved by rotating the reflector position in steps of 120º until completing a circle, thus obtaining an n=3. Finally, the methodology uncertainty (U_{Meth}) quantifies the global reproducibility of the methodology described in this work. To calculate it, three samples (n=3) prepared in parallel were analysed. Figure 7 shows a graphical sampling process used to estimate the method's uncertainties.

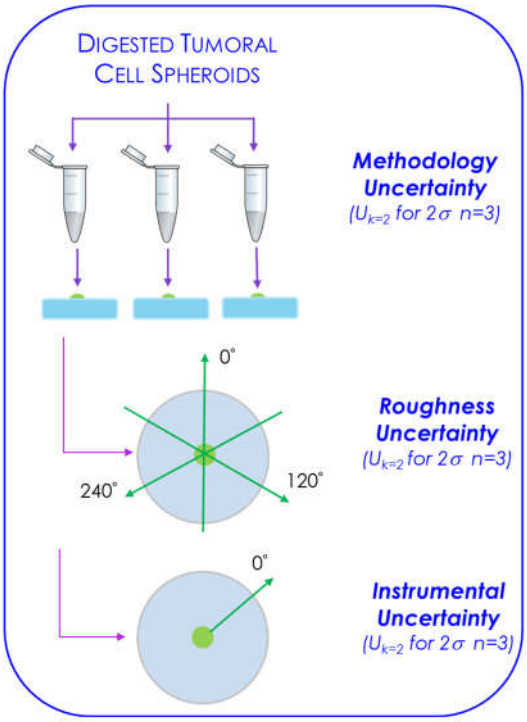

Figure 7. Sampling process used to estimate the three methodologies' uncertainty sources: methodology, roughness, and instrumental uncertainties.

The expanded uncertainties obtained for a sample containing five glioblastoma spheroids exposed to 750 ppm of CaF_2:Nd^{3+},Y^{3+} NPs are shown in Table 3.

Table 3. Methodological, roughness and instrumental expanded uncertainties obtained for the elements evaluated in the TXRF quantifications.

Element	U_{Meth} (%)	U_{Rough} (%)	U_{Ins} (%)
Ca	3.12	1.1	1.1
Y	4.20	2.5	1.6
Nd	9.60	6.8	6.0
P	9.40	6.3	1.8
S	10.60	6.8	4.1
K	4.43	3.3	0.8
Fe	8.51	3.6	6.5
Cu	14.56	3.4	4.2
Zn	13.98	2.4	4.0
Mean ± sd	*10.2 ± 4.1*	*4.3 ± 2.1*	*3.5 ± 2.1*

 doi:10.20944/preprints202602.1118.v1

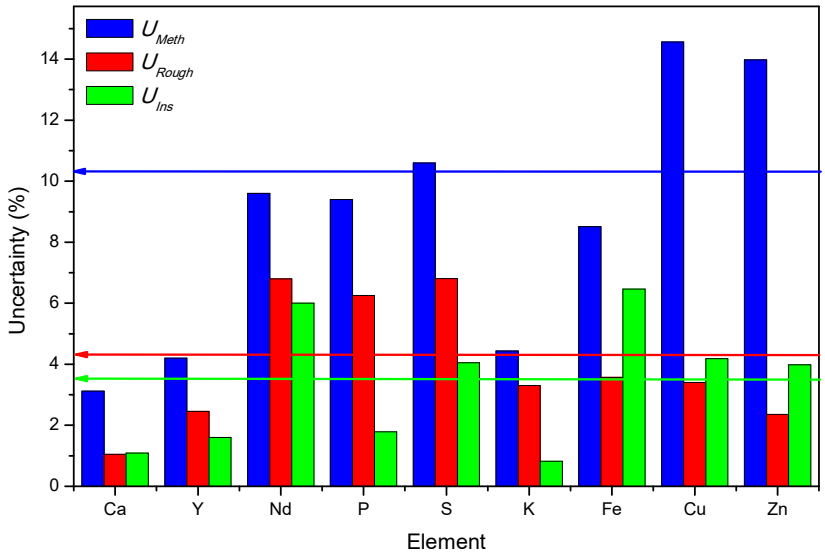

Figure 8. Uncertainties obtained for each element and for each expanded uncertainty are shown. Arrows indicate the average values for methodology (blue), roughness (red), and instrumental (green).

Figure 8 presents a global view of the uncertainties obtained for this TXRF protocol, including the three elements associated with the nanoparticles (Ca, Y, and Nd) and the elements related to the cellular composition (P, S, K, Fe, Cu, and Zn). Their methodological, roughness and instrumental uncertainties are displayed. The arrows indicate the average uncertainties for the methodological (blue), roughness (red), and instrumental (green) components. In this study, the average behaviour uncertainties vary as

$$10.2 \pm 4.1 > 4.3 \pm 2.1 > 3.5 \pm 2.1 \Rightarrow \bar{U}_{Meth} > \bar{U}_{Rough} > \bar{U}_{Ins} \quad (3)$$

This trend aligns with the expected behaviour of the evaluated uncertainty sources, as observed in Equation (3). In fact, it was also reported recently in the analysis of soils using the suspension-assisted TXRF (SA/DSA-TXRF) methodology [35]. Nevertheless, the local trend of the trace elements Fe, Cu and Zn differs from the average behaviour shown in Equation (3), with $U_{Ins} > U_{Rough}$ for all three elements (see Figure 7). This is a surprising fact from a sampling perspective, which may be due to the non-homogeneous 3D distribution of the TXRF depositions, as shown in Figure 9. Additionally, the low concentrations of these elements in the ppb range can increase variability, in combination with the roughness of the deposition, leading to this anomalous behaviour.

Figure 9. Left: optical microscope image of 10 µL deposition of a control sample of U-87 MG spheroids. Right: 3D projection of the same image made with the software 3D Builder.

 doi:10.20944/preprints202602.1118.v1

Figure 9 (left) displays an optical microscopy image of a final deposition of 10 µL of an analysed control sample of glioblastoma. Figure 8 (right) displays a 3D projection of the same image, generated using 3D Builder software, to better illustrate the complex, rough morphology of the TXRF deposition. The Z-axis was derived from the grey-scale values of the original image. Thus, it does not match the deposition thickness at each XY point, but it helps visualise their differences. Figure 9 (right) shows a pronounced volcano effect with a coffee-ring edge and significant thickness differences depending on the angle of rotation of the deposit relative to the incident X-ray beam. This fact supports the previous explanation of the anomalous variability observed for trace elements.

3.3.5. Verification of the Deposition Chemical Homogeneity

One of the most critical aspects of quantitation by TXRF is ensuring that the elemental spatial distributions of the analytes under evaluation and the IS element are comparable. To assess this analytical aspect, µ-XRF was used to analyse the same depositions of the U-87 MG sample shown in Figure 9.

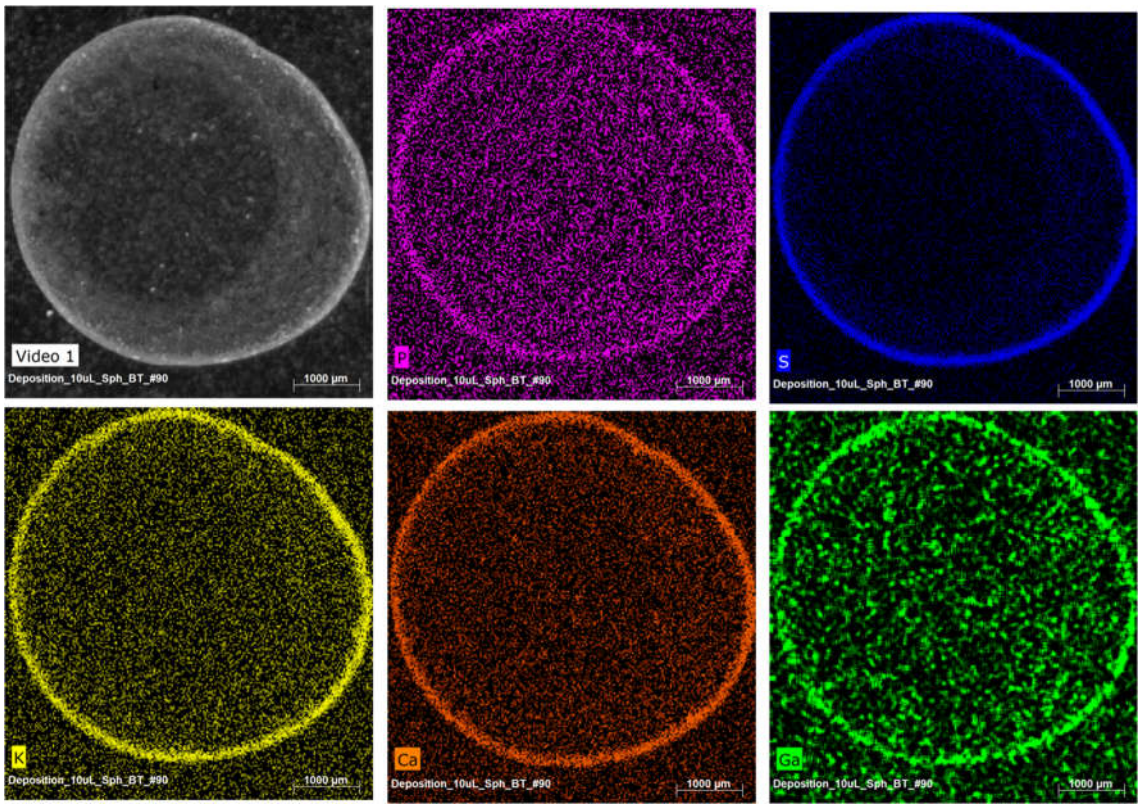

Figure 10. Spatial colocalisation of some elements associated with the glioblastoma spheroids next to the Ga used as an IS in three different residues deposited over a TXRF quartz reflector.

Figure 10 presents a 2D elemental map of the most representative elements of the cellular composition (P, S, K, and Ca) and of Ga, used as the IS, shown individually in each image. In summary, all elements are distributed in a ring shape, which colocalises them with the IS, thereby avoiding quantitative distortions in TXRF measurements due to spatial heterogeneous distribution.

3.4. Uptake of CaF_2:Nd^{3+},Y^{3+} NPs Experiments Results

Once the TXRF methodology was validated, the protocol was applied to investigate the intracellular diffusion of CaF_2:Nd^{3+},Y^{3+} NPs in U-87 MG and MCF-7 spheroids. For each cell line, the NPs concentration and exposure time parameters were investigated.

 doi:10.20944/preprints202602.1118.v1

3.4.1. Spheroids Uptake Versus Nanoparticles Concentration

As described in Section 2.2, four different NP exposure concentrations were tested on the spheroids. Based on the quantification of Nd, and Y, the concentrations of nanoparticles measured in the spheroids are plotted in Figure 11a for both cell lines. Note that the data has been normalised by the number of spheroids in the sample; thus, we are measuring an average intake value.

From these data, cellular uptake was calculated as a percentage, as

$$Cellular\ Uptake\ \% \ = \ 100\ x \frac{C_{NP}\ (\frac{\mu g}{Sph.mL})}{C_0(\mu g/mL)}, \tag{4}$$

where C_{NP} represents the concentration of internalised NPs per spheroid, and C_0 is the starting concentration of NPs used during incubation.

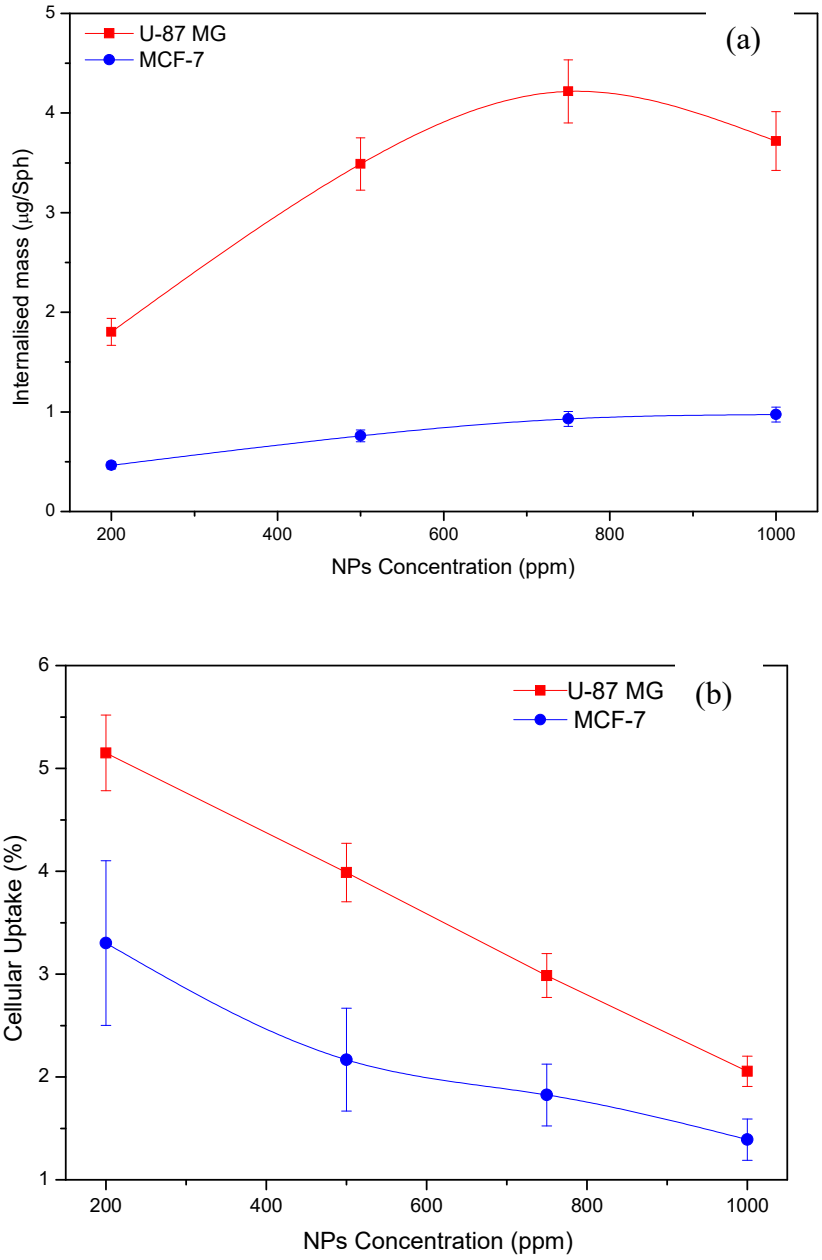

Figure 11. (a) Internalisation mass per spheroid and (b) cellular uptake of $CaF_2:Nd^{3+},Y^{3+}$ NPs for U-87 MG (red) and MCF-7 (blue) spheroids versus NPs concentration added to the cell medium.

The results presented in Figure 11 reveal significant differences in the interaction of $CaF_2:Nd^{3+}$, Y^{3+} NPs with each cell line. The internalisation of the NPs is more significant for U-87 MG

 doi:10.20944/preprints202602.1118.v1

glioblastoma spheroids than for MCF-7 adenocarcinoma ones (Figure 11a), reaching a four-fold increase when 750 ppm NPs are used. In both cases, a saturation effect is observed when a larger number of NPs are added to the culture. If we focus on cellular uptake, U-87 MG spheroids also show greater interaction with NPs than MCF-7 spheroids across all NP dose exposures. However, cellular uptake decreases linearly with the number of NPs added during treatment, meaning that although more NPs interact with cells, a larger fraction remains in the cell culture medium and is washed away.

A possible explanation for the differences between cell lines lies in their distinct 3D morphologies and cell-cell attachment characteristics. The final density of the obtained spheroids depends on the culture method and may vary with a wide range of parameters, including the cell passage and cell medium. In our case, the microscopic comparison of U-87 MG cells form coarse spheroids (see Figure 12 a,b,c), likely more porous than those from MCF-7 cells, which appear as compact, smooth spheres (see Figure 12 d,e,f). This is consistent with the observations of Froehlich et al. [36]. In fact, based on their work and classification, we can consider U-87 MG to be at an intermediate stage between compact aggregates and fully formed spheroids. This becomes clear upon handling them, as U-87 MG cells require longer to form spheroids that can be manipulated without disintegrating.

In addition, U-87 MG spheroids tend to be larger, resulting in a 3 times greater surface area exposed to the surrounding medium, which increases the number of potential contact sites with NPs. As a result, the combined effects of increased porosity, roughness, intercellular spacing, and available surface area enhance nanoparticle biodisponibility for cellular interaction. This structural accessibility increases the probability of nanoparticle–cell interactions and facilitates intracellular diffusion, thereby explaining the higher nanoparticle internalisation observed in U-87 MG spheroids compared to MCF-7 spheroids (Figure 12).

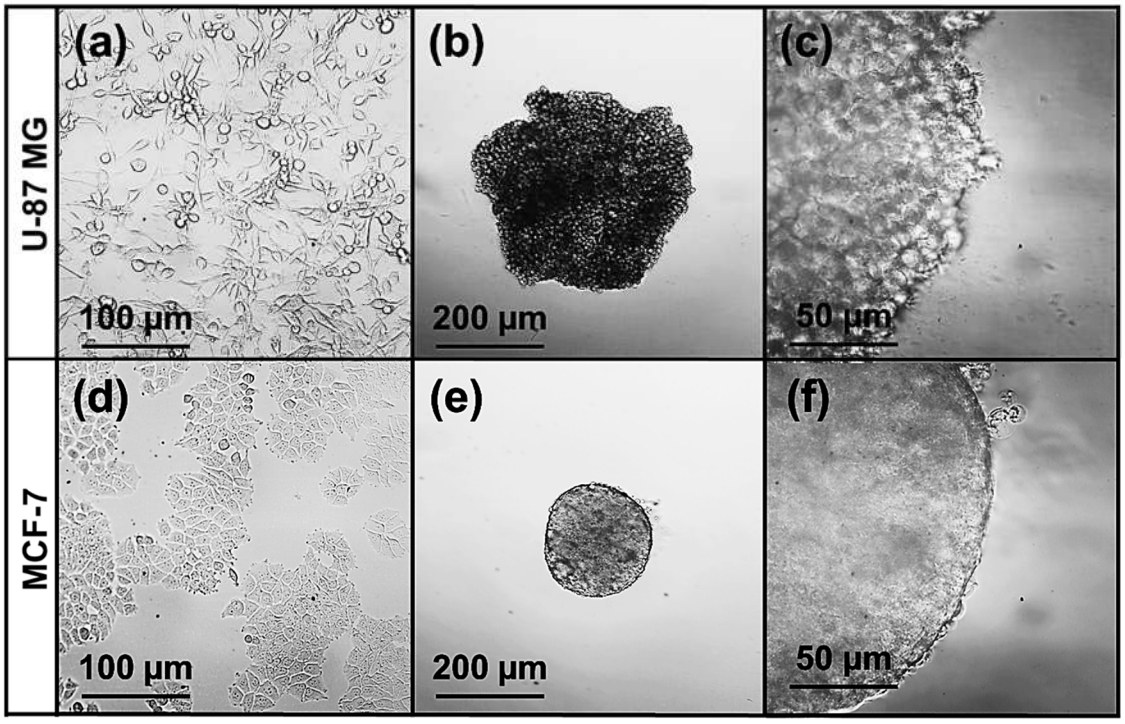

Figure 12. Optical microscopy images of (a) 2D cell cultures of U-87 MG, (b) an spheroid formed from 4.000 cells at day 4 and (c) a higher-magnification view of the spheroid edges. Equivalent optical images obtained for the MCF-7 cell line, including (d) the monolayer culture cells, (e) a spheroid with the same growing conditions and (f) a magnification of the spheroid edge.

 doi:10.20944/preprints202602.1118.v1

3.4.2. Nanoparticle Uptake Versus Time

Spheroids treated with NPs during different time spans were prepared, as described in Section 2.2. Same as in the previous section, from TXRF results, the mass of NPs per spheroid and the cellular uptake were calculated. The obtained values are plotted in Figure 13 for both cell lines.

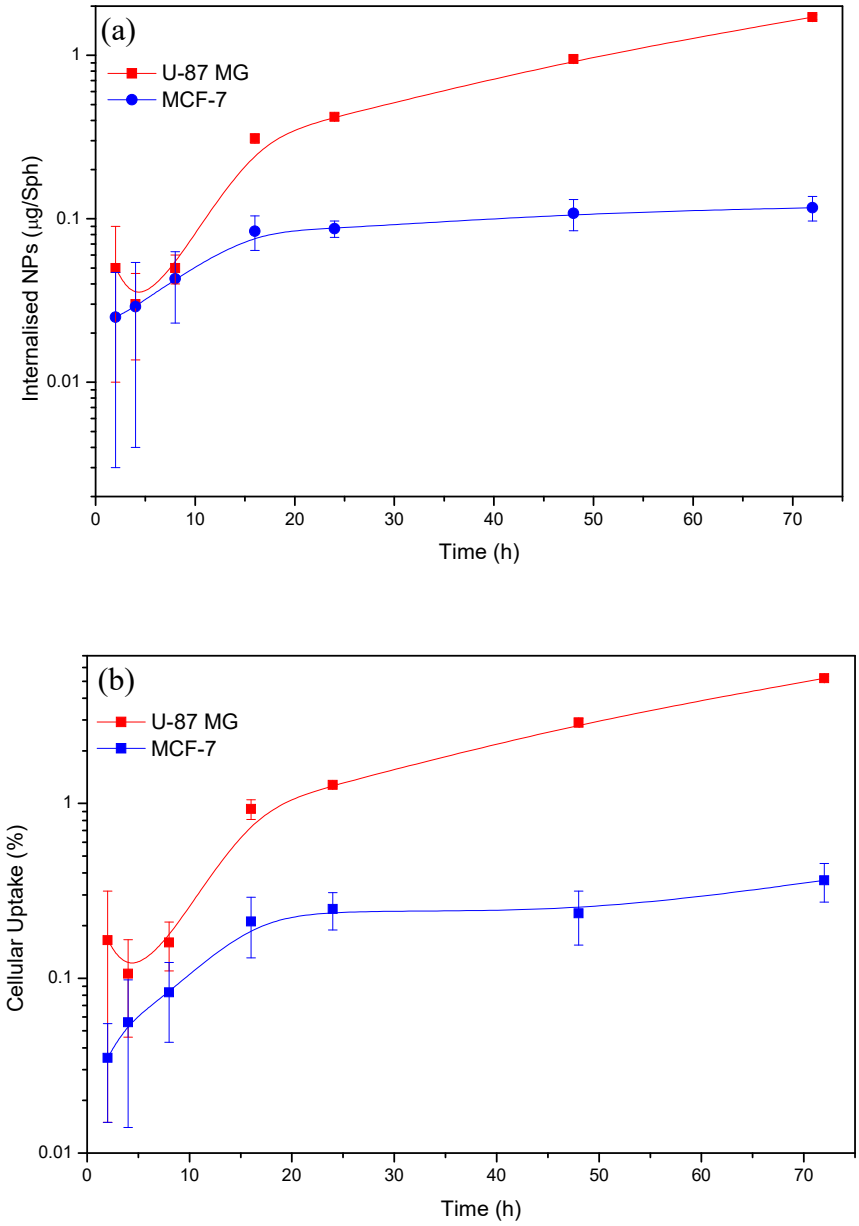

Figure 13. (a) Internalised mass per spheroid and (b) cellular uptake of $CaF_2:Nd^{3+},Y^{3+}$ NPs for U-87 MG (red) and MCF-7 (blue) spheroids versus time of exposure. A continuous line is plotted as a guide for the eye.

Significant differences are again observed when the two cell lines are compared, as both internalisation and cellular uptake of the NPs are higher in U-87 MG than in MCF-7 spheroids. In either case, the logarithmic plot in Figure 13 shows a progressive reduction of the rate at which NPs enter the spheroid. In the case of MCF-7, it has even reached a saturation stage, in which the internalised mass changes little despite longer treatments. This is consistent with a reduction in the NPs concentration in the cell medium over time, due to internalisation, and the increase in NPs concentration, within cells or in the intercellular space, both reaching a limit.

 doi:10.20944/preprints202602.1118.v1

3.4.3. Modelisation of the Diffusion Process

To further characterise the process, the NPs in-diffusion can be fitted to the stretched-exponential function given by the Weibull diffusion model. Widely used in pharmacology to describe complex drug-release kinetics, it is also suitable for systems with radial geometry, such as 3D spheroids. In fact, Carr et al. [37] demonstrated that in such case diffusion is inherently multi-exponential, thus a simple first-order model loses accuracy. Instead, a Weibull function better describes the true diffusive behaviour in a three-parameter compact model. For the cumulative NPs content inside the spheroid as a function of time, the Weibull function can be expressed as:

$$C(t)_{NPs} = C_{\infty}\left(1 - e^{-(t/\tau)^{\beta}}\right), \quad (5)$$

where the parameters C_{∞}, τ and β have the following physical meaning: C_{∞} reflects the maximum nanoparticle load achievable by the spheroid, τ represents the characteristic timescale of the diffusion process and relates to the effective diffusion coefficient and spheroid geometry and finally, β determines the curvature of the kinetic profile and is the most informative descriptor of the underlying transport mechanism. So, values of β lower than 0.7 indicate sub-exponential kinetics, typically dominated by diffusion (linked to Fick's law) behaviours; values of β between 0.7 and 1.1, are close to the exponential behaviour, and indicate anomalous transport, where the global kinetics reflect the combined influenceof several processes; finally, values of β higher than 1.1 indicate the presence of an accelerated NPs transport, approaching sigmoidal kinetics, deviating from simple diffusion and reflecting the dominance of additional uptake or transport processes [38].

Figure 14 shows the nonlinear least-squares fit of the Weibull model (Equation (5)) performed, weighted by the standard deviation of the internalised NPs concentration data in U-87 MG and MCF-7 spheroids.

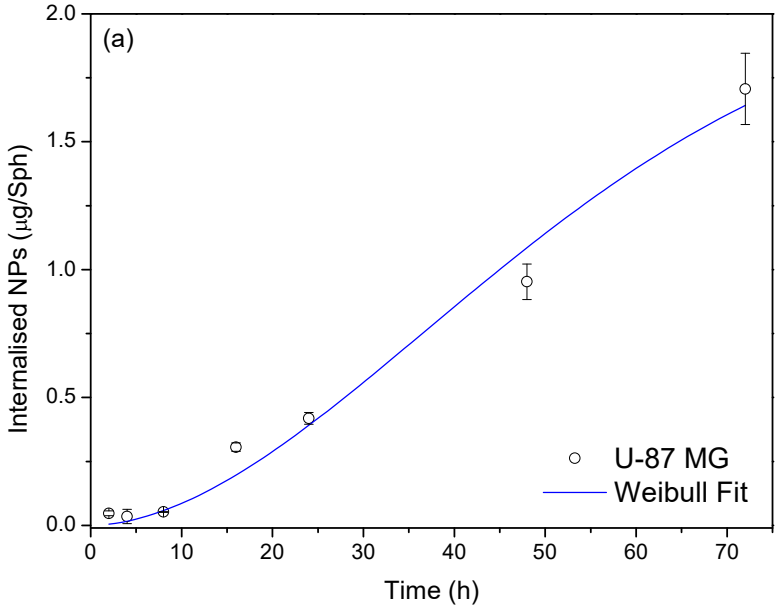

 doi:10.20944/preprints202602.1118.v1

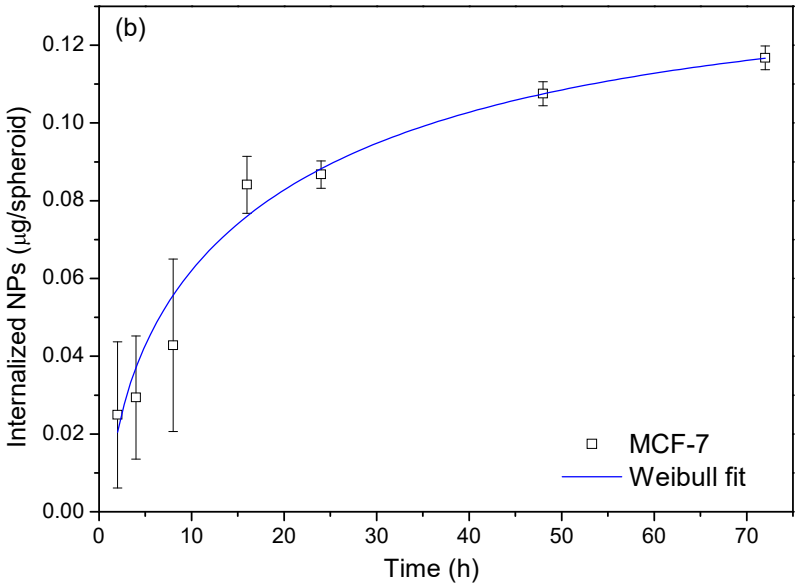

Figure 14. Internalisation of CaF_2:Nd^{3+}, Y^{3+} NPs in (a) U-87 MG and (b) MCF-7 spheroids versus treatment time of exposure. Weibull fit modelis shown in a blue line.

As shown in Figure 14, the Weibull model describes reasonably well the diffusion kinetics of NPs in spheroids. In the case of the U-87 MG spheroids (Figure 14a), the absence of a clear saturation within the experimental window reduces the robustness of the fit. Nevertheless, the obtained parameters are self-consistent: C_∞=2.1 ± 1.6 µg/Sph, τ = 57 ± 13 h and β = 1.82 ± 0.12. These parameter sets reveal accelerated kinetics, consistent with a globally sigmoidal profile, rather than a simple first-order behaviour. Although the saturation range was not reached, the larger C_∞ and longer τ values suggest a greater internalisation ability than in MCF-7 spheroids. In the case of the MCF-7 spheroids (Figure 14b), the fitted parameters were C_∞=0.13 ± 0.03 µg/Sph, τ = 19 ± 12 h and β = 0.68 ± 0.40. These values indicate sub-exponential (anomalous) kinetics, typically associated with diffusion-dominated behaviours. Consistent with this, the data indicate a relatively slow uptake, with only a modest fraction of the administered NPs dose retained within the spheroid at equilibrium.

4. Conclusions

The work demonstrated that TXRF spectrometry is a powerful, practical, rapid, and accurate analytical method for determining trace and rare-earth elements at low concentrations during the internalisation of nanoparticles in 3D cellular systems. In particular, this is demonstrated for CaF_2: Nd^{3+}, Y^{3+} nanoparticles in U-87 MG and MCF-7 spheroids.

Beyond compositional elements of the investigated NPs (Ca, Nd, Y), TXRF enables highly sensitive quantification of cellular trace metal content (P, S, K, Ca, Fe, Cu, Zn) in low-volume biological samples, thereby validating its microanalytical character and its use for nanoparticle tracking quantification in 3D cancer model assessment. A protocol for the microdigestion of the evaluated exposed spheroids to NPs was developed, including a home-made digestion system for these microsamples.

The methodology was validated by evaluating average concentrations, within the range between 50 ppb (ng/mL) for Cu up to 27.46 ppm (µg/mL) for P, and detection limits (*DLs*) within the range between 11 ppb for Cu and 1.11 ppm for P. The coefficient of variation was always below 1.85 %. The expanded uncertainty sources were evaluated, including the developed methodology (U_{Meth} ~10.2 ± 4.1 %), the deposition roughness (U_{Rough} ~4.3 ± 2.1 %), and the instrumental (U_{Ins} ~3.5 ± 2.1 %). Finally, recoveries relative to the theoretical composition of the investigated NPs were also evaluated, yielding values of approximately 100%. The analytical recoveries obtained by the spike

 doi:10.20944/preprints202602.1118.v1

method remained around 100 %, confirming the validity and robustness of the developed method and TXRF spectrometry. In conclusion, accuracy was confirmed through near-100% recoveries, low uncertainty was achieved, and the absence of matrix interference was validated, reinforcing TXRF's reliability for this application.

The method has been applied to study the diffusion processes of $CaF_2:Nd^{3+}$, Y^{3+} NPs, evaluating two main parameters: time and exposure concentration. The study has demonstrated higher NPs bioaccumulation in U-87 MG spheroids than in MCF-7 spheroids regardless of the concentration of NPs applied, reaching 4-fold higher values. In experiments performed at different treatment times, a saturation effect was observed, which can be described phenomenologically by a Weibull model. In MCF-7 spheroids, the fitted parameters (C_∞=0.13 ± 0.03 μg/Sph, τ = 19 ± 12 h and β = 0.68 ± 0.40) fall within the range associated with sub-exponential (anomalous) kinetics in spherical systems, consistent with diffusion-limited uptake that results in a modest accumulation of NPs. In U-87 MG spheroids, the fitted parameters (C_∞=2.1 ± 0.6 μg/Sph, τ = 57 ± 13 h and β = 1.82 ± 0.12) suggest an accelerated regime. Although saturation was not reached within the experimental timeframe, substantial nanoparticle accumulation was observed throughout the spheroid. The differences suggest cell-line-dependent uptake behaviour, potentially influenced by differences in spheroid cellular architecture, including roughness and porosity, as well as intercellular 3D microstructure. A higher active area in U-87 MG spheroids than in MCF-7 spheroids, related to their apparent roughness and porosity, may explain the observed differences. To confirm this explanation, additional measurements of the surface morphology of the 3D spheroids should be performed to quantify their effective area.

The study focuses exclusively on two representative cell lines, U-87 MG (glioblastoma) and MCF-7 (adenocarcinoma), grown as 3D spheroids. Spheroids better replicate tumour microstructure and cell metabolism than 2D cultures, enabling realistic evaluation of nanoparticle-cell interactions for nanotheranostic applications while remaining simplified in vitro systems. These results indicate the need for more extensive research lines on biosystems closest to the real tumour, such as 3D spheroids, before taking a future in vivo step, if the research so indicates.

The study focuses exclusively on two representative cell lines, U-87 MG (glioblastoma) and MCF-7 (breast adenocarcinoma), grown as 3D spheroids. Spheroids better replicate tumour microstructure and cell metabolism than 2D cultures, enabling realistic evaluation of nanoparticle-cell interactions for nanotheranostic applications while remaining simplified in vitro systems. These results indicate the need for more extensive research lines on biosystems closest to the real tumour, such as 3D spheroids, before taking a future in vivo step, if the research so indicates.

Author Contributions: Conceptualisation, R.F-R. and P.M.L.; methodology, R.F-R. and P.M.L; software, P.M.L., R.F-R. and M.Q.M.; validation, R.F-R., P.M.L. P.H-G. and M.Q.M; formal analysis, R.F-R., P.M.L.; investigation, P.M.L, R.F-R and M.Q.M.; resources, M.Q.M. and P.H-G.; data curation, R.F-R., P.M.L. and M.Q.M.; writing—original draft preparation, R.F-R., P.M.L. and M.Q.M.; writing—review and editing, R.F-R., P.M.L. and M.Q.M.; visualisation, X.X.; supervision, P.M.L, R.F-R., P.H-G. and M.Q.M.; project administration, M.Q.M and P. H-G.; funding acquisition, M.Q.M and P. H-G. All authors have read and agreed to the published version of the manuscript.

Funding: This research was funded by the Ministry of Science, Innovation and Universities of Spain, through grant EQC2021-007386-P and under the project CNS2023-145169 SAHNDOCAN, funded by MCIN/AEI/10.13039/50xs1100011033 and by the European Union NextGenerationEU/PRTR.

Institutional Review Board Statement: Not applicable.

Informed Consent Statement: Not applicable.

Data Availability Statement: The raw data supporting the conclusions of this article will be made available by the authors on request.

 doi:10.20944/preprints202602.1118.v1

Acknowledgments: The authors wish to express their gratitude to the Universidad Autónoma de Madrid (UAM) for technical support and to the laboratory technician at the XRF-Lab of the SIdI-UAM centre for their assistance with the experiments. The authors would like to acknowledge Dr. Malou Henriksen-Lacey and Prof. Luis Liz-Marzán, from CIC BiomaGUNE (San Sebastián, Spain), for supplying the cell lines.

Conflicts of Interest: The authors declare no conflict of interest.

References

1. Zhao, H.; Xiao, H.; Liu, Y.; Ju, H. Lanthanide-doped rare earth nanoparticles for near-infrared-II imaging and cancer therapy. *BMEMat* **2023**, *1*, https://doi.org/10.1002/bmm2.12032.
2. Camarero, P.; López-Méndez, R.; Díez, D.L.; Haro-González, P.; Cantelar, E.; Quintanilla, M. The Role of Optical Centers in Neodymium-Doped Calcium Fluoride: Optical Tagging and Nanothermometry in the Second Biological Window. *Adv. Opt. Mater.* **2025**, *13*, https://doi.org/10.1002/adom.202501200.
3. Quintanilla, M.; García, I.; de Lázaro, I.; García-Alvarez, R.; Henriksen-Lacey, M.; Vranic, S.; Kostarelos, K.; Liz-Marzán, L.M. Thermal monitoring during photothermia: hybrid probes for simultaneous plasmonic heating and near-infrared optical nanothermometry. *Theranostics* **2019**, *9*, 7298–7312, https://doi.org/10.7150/thno.38091.
4. Arora, S.; Singh, S.; Mittal, A.; Desai, N.; Khatri, D.K.; Gugulothu, D.; Lather, V.; Pandita, D.; Vora, L.K. Spheroids in cancer research: Recent advances and opportunities. *J. Drug Deliv. Sci. Technol.* **2024**, *100*, https://doi.org/10.1016/j.jddst.2024.106033.
5. Klockenkämper, R.; Von Bohlen, A. Total-Reflection X-Ray Fluorescence Analysis and Related Methods, 2nd ed.; John Wiley & Sons: Hoboken, NJ, USA, 2015.
6. Fernández-Ruiz, R.; Furió, M.; Galisteo, F.C.; Larese, C.; Granados, M.L.; Mariscal, R.; Fierro, J.L.G. Chemical Analysis of Used Three-Way Catalysts by Total Reflection X-ray Fluorescence. *Anal. Chem.* **2002**, *74*, 5463–5469, https://doi.org/10.1021/ac025927r.
7. Fernández-Ruiz, R.; Galisteo, F.C.; Larese, C.; Granados, M.L.; Mariscal, R.; Fierro, J.L.G. TXRF analysis of aged three way catalysts. *Anal.* **2006**, *131*, 590–594, https://doi.org/10.1039/b513508g.
8. Magalhães, T.; von Bohlen, A.; Carvalho, M.; Becker, M. Trace elements in human cancerous and healthy tissues from the same individual: A comparative study by TXRF and EDXRF. *Spectrochim. Acta Part B: At. Spectrosc.* **2006**, *61*, 1185–1193, https://doi.org/10.1016/j.sab.2006.06.002.
9. von Czarnowski, D.; Denkhaus, E.; Lemke, K. Determination of trace element distribution in cancerous and normal human tissues by total reflection X-ray fluorescence analysis. *Spectrochim. Acta Part B: At. Spectrosc.* **1997**, *52*, 1047–1052, https://doi.org/10.1016/s0584-8547(96)01625-4.
10. Ruiz, R.F.; Tornero, J.D.; González, V.M.; Alonso, C. Quantification of Pt bound to DNA using total-reflection X-ray fluorescence (TXRF). *Anal.* **1999**, *124*, 583–585, https://doi.org/10.1039/a900725c.
11. Mauricio González, Lucía Tapia, Milton Alvarado, J. D. Tornero and R. Fernández-Ruiz. Intracellular determination of elements in mammalian cultured cells by total reflection X-ray fluorescence spectrometry. J. Anal. At. Spectrom., 1999, 14, 885–888.
12. Levcenko, S.; Syrbu, N.N.; Arushanov, E.; Tezlevan, V.; Fernández-Ruiz, R.; Merino, J.M.; León, M. Optical properties of monocrystalline CuIn5Se8.CONFERENCE NAME, LOCATION OF CONFERENCE, COUNTRYDATE OF CONFERENCE; p. 073513.
13. Krämer, M.; von Bohlen, A.; Sternemann, C.; Paulus, M.; Hergenröder, R. Synchrotron radiation induced X-ray standing waves analysis of layered structures. *Appl. Surf. Sci.* **2006**, *253*, 3533–3542, https://doi.org/10.1016/j.apsusc.2006.07.076.
14. Fernández-Ruiz, R.; Cabañero, J.P.; Hernández, E.; León, M. Determination of the stoichiometry of CuxInySez by total-reflection XRF. *Anal.* **2001**, *126*, 1797–1799, https://doi.org/10.1039/b104466b.
15. Cariati, F.; Fermo, P.; Gilardoni, S.; Galli, A.; Milazzo, M. A new approach for archaeological ceramics analysis using total reflection X-ray fluorescence spectrometry. *Spectrochim. Acta Part B: At. Spectrosc.* **2003**, *58*, 177–184, https://doi.org/10.1016/s0584-8547(02)00253-7.

 doi:10.20944/preprints202602.1118.v1

16. Fernández-Ruiz, R.; Garcia-Heras, M. Analysis of archaeological ceramics by total-reflection X-ray fluorescence: Quantitative approaches. *Spectrochim. Acta Part B: At. Spectrosc.* **2008**, *63*, 975–979, https://doi.org/10.1016/j.sab.2008.06.004.
17. Maltsev, A.S.; Pashkova, G.V.; Fernández-Ruiz, R.; Demonterova, E.I.; Shuliumova, A.N.; Umarova, N.N.; Shergin, D.L.; Mukhamedova, M.M.; Chubarov, V.M.; Mikheeva, E.A. Characterization of archaeological ceramics from eastern Siberia by total-reflection X-ray fluorescence spectrometry and principal component analysis. *Spectrochim. Acta Part B: At. Spectrosc.* **2021**, *175*, https://doi.org/10.1016/j.sab.2020.106012.
18. Klockenkämper, R.; von Bohlen, A. Determination of the critical thickness and the sensitivity for thin-film analysis by total reflection X-ray fluorescence spectrometry. *Spectrochim. Acta Part B: At. Spectrosc.* **1989**, *44*, 461–469, https://doi.org/10.1016/0584-8547(89)80051-5.
19. R. Klockenkämper and A. Von Bohlen. Survey of sampling techniques for solids suitable for microanalysis by total-reflection X-ray fluorescence spectrometry. J. Anal. At. Spectrom., 1999, 14, 571-576.
20. Fernández-Ruiz, R.; Costo, R.; Morales, M.; Bomatí-Miguel, O.; Veintemillas-Verdaguer, S. Total-reflection X-ray fluorescence: An alternative tool for the analysis of magnetic ferrofluids. 12th International Conference on Total Reflection X-Ray Fluorescence Analysis and Related Methods. LOCATION OF CONFERENCE, COUNTRYDATE OF CONFERENCE; pp. 1387–1394.
21. Fernández-Ruiz, R.; Redrejo, M.J.; Friedrich, E.J.; Ramos, M.; Fernández, T. Evaluation of Bioaccumulation Kinetics of Gold Nanorods in Vital Mammalian Organs by Means of Total Reflection X-Ray Fluorescence Spectrometry. *Anal. Chem.* **2014**, *86*, 7383–7390, https://doi.org/10.1021/ac5006475.
22. Peschel, B.U.; Fittschen, U.E.A.; Pepponi, G.; Jokubonis, C.; Streli, C.; Wobrauschek, P.; Falkenberg, G.; Broekaert, J.A.C. Direct analysis of Al2O3 powders by total reflection X-ray fluorescence spectrometry. *Anal. Bioanal. Chem.* **2005**, *382*, 1958–1964, https://doi.org/10.1007/s00216-005-3295-0.
23. Fernández-Ruiz, R. TXRF spectrometry in the bioanalytical sciences: A brief review. *X-Ray Spectrom.* **2021**, *51*, 279–293, https://doi.org/10.1002/xrs.3243.
24. Fernández-Ruiz, R. Bioanalytical Application of the Total-Reflection X-Ray Fluorescence Spectrometry. *Int. J. Mol. Sci.* **2025**, *26*, 1049, https://doi.org/10.3390/ijms26031049.
25. Mankovskii, G.; Pejović-Milić, A. Quantification of gold nanoparticles in blood using total reflection X-ray fluorescence. *Spectrochim. Acta Part B: At. Spectrosc.* **2022**, *194*, https://doi.org/10.1016/j.sab.2022.106466.
26. Hedden, N.; Traplin, G.; Mankovskii, G.; Karshafian, R.; Kolios, M.; Pejovic-Milic, A. Quantifying Cytotoxicity and Cellular Uptake of Naked Gold Nanoparticles Using Total Reflection X-Ray Fluorescence. *X-Ray Spectrom.* **2025**, https://doi.org/10.1002/xrs.70006.
27. Traplin, G.; Karshafian, R.; Pejovic-Milic, A. Total X-Ray Fluorescence Measurement of Spherical Gold Nanoparticle Uptake by PC -3 Cells: Dual-Phase Kinetic Uptake and Modelling. *X-Ray Spectrom.* **2025**, *55*, 210–222, https://doi.org/10.1002/xrs.70041.
28. Mankovskii, G.; Pejović-Milić, A. Quantification of gold nanoparticles in histologically thin tissue slices using TXRF. *X-Ray Spectrom.* **2021**, *51*, 271–278, https://doi.org/10.1002/xrs.3271.
29. Pedrosa, P.; Baptista, P.V.; Fernandes, A.R.; Guerra, M. Benchtop X-ray fluorescence imaging as a tool to study gold nanoparticle penetration in 3D cancer spheroids. *RSC Adv.* **2021**, *11*, 26344–26353, https://doi.org/10.1039/d1ra05446e.
30. Burattini, E.; Cinque, G.; Bellisola, G.; Fracasso, G.; Monti, F.; Colombatti, M. Synchrotron Radiation μ-X Ray Fluorescence on Multicellular Tumor Spheroids. X-RAY AND INNER-SHELL PROCESSES. LOCATION OF CONFERENCE, ItalyDATE OF CONFERENCE; pp. 515–521.
31. Pedroni, M.; Piccinelli, F.; Passuello, T.; Giarola, M.; Mariotto, G.; Polizzi, S.; Bettinelli, M.; Speghini, A. Lanthanide doped upconverting colloidal CaF2 nanoparticles prepared by a single-step hydrothermal method: toward efficient materials with near infrared-to-near infrared upconversion emission. *Nanoscale* **2011**, *3*, 1456–1460, https://doi.org/10.1039/c0nr00860e.
32. Thakur, D.; Dubey, N.P.; Singh, R. A Review on Spike and Recovery Method in Analytical Method Development and Validation. *Crit. Rev. Anal. Chem.* **2022**, *54*, 2053–2071, https://doi.org/10.1080/10408347.2022.2152275.

 doi:10.20944/preprints202602.1118.v1

33. Fernández-Ruiz, R. Uncertainty in the Multielemental Quantification by Total-Reflection X-ray Fluorescence: Theoretical and Empirical Approximation. *Anal. Chem.* **2008**, *80*, 8372–8381, https://doi.org/10.1021/ac800780x.
34. Fernández-Ruiz, R. A brief revision of the suspension-assisted direct solid analysis by TXRF spectrometry. *Spectrochim. Acta Part B: At. Spectrosc.* **2025**, *229*, https://doi.org/10.1016/j.sab.2025.107214.
35. Fernández-Ruiz, R. Different Analytical Approaches to the Soil Analyses by TXRF. *X-Ray Spectrom.* **2025**, *54*, 556–570, https://doi.org/10.1002/xrs.3492.
36. Froehlich, K.; Haeger, J.-D.; Heger, J.; Pastuschek, J.; Photini, S.M.; Yan, Y.; Lupp, A.; Pfarrer, C.; Mrowka, R.; Schleußner, E.; et al. Generation of Multicellular Breast Cancer Tumor Spheroids: Comparison of Different Protocols. *J. Mammary Gland. Biol. Neoplasia* **2016**, *21*, 89–98, https://doi.org/10.1007/s10911-016-9359-2.
37. Carr, E.J. Exponential and Weibull models for spherical and spherical-shell diffusion-controlled release systems with semi-absorbing boundaries. *Phys. A: Stat. Mech. its Appl.* **2022**, *605*, https://doi.org/10.1016/j.physa.2022.127985.
38. Martín-Camacho, U.d.J.; Rodríguez-Barajas, N.; Sánchez-Burgos, J.A.; Pérez-Larios, A. Weibull β value for the discernment of drug release mechanism of PLGA particles. *Int. J. Pharm.* **2023**, *640*, 123017, https://doi.org/10.1016/j.ijpharm.2023.123017.